Validation of a Discrete-Time-Domain Model of a High-Power Medium-Voltage Resonant Converter

Mahdizadeh Shalmaei, Amir Hossein; N. Soltani, Mohsen; Hajizadeh, Amin

Published in:
IEEE Press

Publication date:
2023

Validation of a Discrete-Time-Domain Model of a High-Power Medium-Voltage Resonant Converter*

Amir Hossein Mahdizadeh Shalmaei[1], Mohsen Soltani[1] and Amin Hajizadeh[1]

Abstract— **The widespread deployment of LLC resonant converters in DC technologies has attached a profound significance to the modeling and controlling of such power converters. Compared to the conventional DC-DC converters that could be modeled through small-signal analysis, the Modeling of the LLC resonant converters is complicated. This complexity comes from the way that the electrical energy in a resonant tank is processed, which leads to high non-linearity. Therefore, small-signal analysis is traditionally performed via empirical approaches or iterative simulation methods at around the resonant frequency. But, the weak spot associated with these methods is that they provide superficial and limited insight into the system's dynamic. Moreover, the accuracy of the model is adversely affected as far as the switching frequency deviates from the resonant frequency. This inaccuracy issue becomes serious when the converter operates in sub-resonant mode as this mode is preferred for medium voltage applications. This article, therefore, presents a discrete-time domain approach through which the model of a medium-voltage LLC resonant is derived. Then, the dynamic and static behaviors of the plant are briefly investigated. Finally, a meaningful comparison between the simulation and experimental results obtained from a scaled prototype is provided to validate the modeling approach.**

Keywords: Medium-voltage DC-DC converters, LLC resonant converter, Behavioral analysis, Discrete-time domain approach.

I. INTRODUCTION

DC technology already plays an undeniable role in all aspects of energy transmission and distribution levels. As a salient instance, projects on high-voltage direct-current (HVDC) grids and micro-grids, set up by R&D, witness the feasibility of the deployment of DC technologies in the near future. One of the requirements to reach the point where a high penetration of DC-distributed energy exists is to utilize high efficiency and high power density medium-voltage DC-DC (MVDC) converters. As shown in Fig. 1, MVDC converters, as the power collection unit in offshore wind farms, are a key part that is recently offered to be substituted with the conventional AC-based power collection stage. This, as a consequence, results in a more compact size, fewer energy costs, and higher efficiencies [1].

Among various sorts of DC-DC converters that fulfill the criteria for this application, the series LLC resonant converters demonstrated in Fig. 2 seem to be potential candidates due to their unique features. High efficiency, high power density, low Electro-Magnetic Interference (EMI), and soft switching capability are merely some of the prominent attributes that could be mentioned [2], [3]. Despite these enticing characteristics, the modeling and control of this converter are complicated. This complexity stems from the changes in dynamic and static behaviors of the resonant converter for different switching frequencies; that is, obtaining a unique model that can describe the behavior of the system for a wide range of switching frequencies is cumbersome [4], [5]. A definite number of approaches with the purpose of addressing this barrier have been suggested up to now.

A modified method based on communication theory is proposed by [6]. By this method, a control-to-output transfer function is derived. But the weak spot with this approach is the inaccuracy of the model for lower frequencies. To tackle the inaccuracy issue of this strategy, a new approach called Virtual Network Analyzer (VNA) is presented by [7]. The accuracy of this method, however, is relatively high, it suffers from a long simulation time. Compared to VNA, sampled-data modeling suggested by [7] is another approach that is fast; although the accuracy of the obtained model deteriorates for higher frequencies. Moreover, extreme numerical and analytical efforts would be needed for converters with more operating modes. As suggested by [8], First Harmonic Approximation (FHA) is another approach that approximates the converter based on the fundamental frequency. In spite of the fact that the model derived from this strategy accurately describes the dynamic and static behaviors of the system when the converter operates at the resonant frequency, the accuracy becomes worse for the switching frequencies further than the resonant frequency. In Contrast to this method that only considers the first harmonic, modeling based on Extended Describing Function (EDF) suggested by [9], [10] accurately approximates the nonlinear behavior of the system through the Fourier series. This method is accurate but tedious as obtaining small signal equivalent circuits for nonlinear elements is tough.

Another time domain-based approach through which the dynamic model of the resonant converter could be extracted is called discrete-time domain modeling [11]. In this method, the state variables are computed at the commencement of each switching cycle. The discrete-time domain modeling concept later is used by [12] to derive the mathematical model of a pulse-removal-technique-based Series Resonant Converter (SRC). But, neither is the dynamic model of SRC investigated nor is it used to design a controller.

Hence, this study aims to address these issues; that is, modeling an SRC by discrete time domain modeling approach and investigating the obtained model from dynamic

*This work was partially supported by AAU Energy, EUDP project no. 640222-496821, and Energy Cluster Denmark under project W-Tools.

[1] Authors are with the department of AAU Energy, Aalborg University, Esbjerg, Denmark ahms@energy.aau.dk sms@energy.aau.dk, and aha@energy.aau.dk

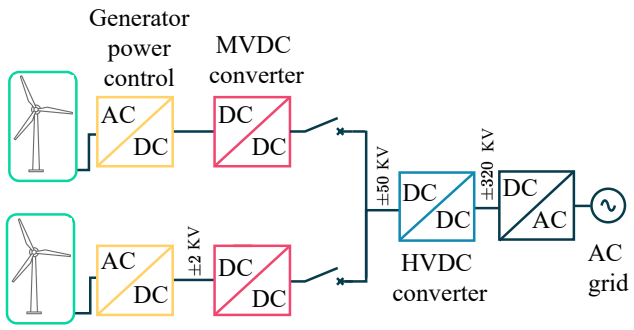

Fig. 1. Single line architecture of a DC wind farm.

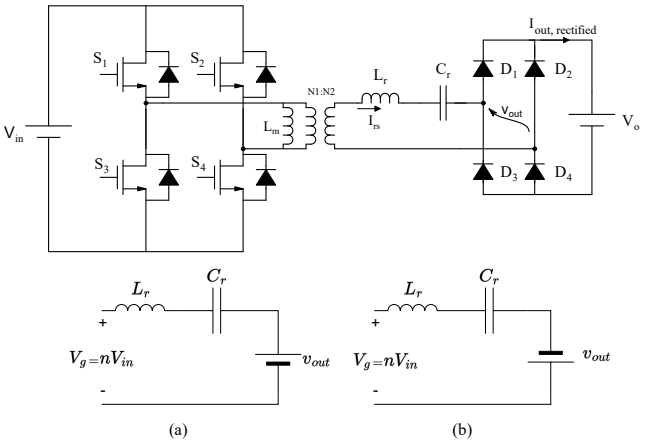

Fig. 2. A layer of series LLC resonant converter (SRC).

and static points of view. Then, a gain-scheduled PI controller that ensures the stability and consistent performance of the plant over a wide range of operating frequencies is designed.

This paper is organized as: The Large-signal analysis of the SRC is conducted in section (II) after which small signal analysis is presented in section (III). The experimental results are compared to the simulation results in section (IV). Eventually, the study conducted in this paper is wrapped up in the conclusion.

II. TIME DOMAIN EQUATIONS OF THE SRC

As depicted in Fig. 2, the SRC consists of a full bridge inverter, a transformer, a resonant tank, and a full bridge rectifier. To analyze the SRC, the following assumptions are made.

- All components including passive and active ones shown in Fig. 2 are ideal.
- The output voltage maintains constant due to its connection to the grid.
- The converter is assumed to function in the sub-resonant mode owing to the ZCS capability which is preferred in medium-voltage applications.
- Under steady-state circumstances, the SRC has four operating modes in each switching cycle, but owing to the similarity of waveforms in two halves, only the first two operating modes are analyzed.

In what follows, two operating modes of the SRC along with their equivalent circuits, shown in Fig. 2(a) and Fig. 2(b), and key waveforms, shown in Fig. 3, are provided in detail.

ModeI [t_0 t_1]: As shown in Fig. 2, this mode of operation occurs when the diagonal active switches S1 and S4 are turned on. As a result, the primary side of the transformer is connected to the input voltage source Vin, making resonant inductor Lr and resonant capacitor Cr resonate. In other words, a sinusoidal current passes through the resonant tank. By applying Kirchhoff's law to the equivalent circuit demonstrated in Fig 2. a, the differential equations are obtained.

$$V_g = L_r \frac{dI_{rs}(t)}{dt} + v_{Cr}(t) + v_{out}(t), \tag{1}$$

$$I_{rs}(t) = C_r \frac{dv_{Cr}(t)}{dt}, \tag{2}$$

where V_g, V_{Cr} and v_{out} are, respectively, the input voltage transferred to the secondary side of the transformer, the voltage placed across the resonant capacitor, and the input voltage of the rectifier. Meanwhile, I_{rs} is the current flowing through the secondary side of the transformer with the turn ratio of n. By solving (1), the 3 are derived.

$$I_{rs}(t) = \frac{V_g - v_{Cr0} - v_{out}}{z_r} sin(w_r t) + I_{rs0} cos(w_r t), \tag{3}$$

$$\begin{aligned} v_{Cr}(t) = &-(V_g - v_{Cr0} - v_{out}) cos(w_r t) \\ &+ I_{rs0} z_r sin(w_r t) + V_g - v_{out}, \end{aligned} \tag{4}$$

$$w_r = \frac{1}{\sqrt{L_r C_r}}, \tag{5}$$

$$z_r = \sqrt{\frac{L_r}{C_r}}, \tag{6}$$

where v_{Cr0} and v_{out}, respectively, represent the initial capacitor voltage and the alternating output voltage before being rectified. I_{rs0} similarly shows the initial resonant inductor current. Furthermore, ω_r and Z_r denote the resonant frequency and characteristic impedance, respectively. As the converter operates in the sub-resonant mode, this mode of operation ends once the inductor current I_{rs} meets zero.

$$t_1 = \frac{1}{w_r} \left[tan^{-1}\left(\frac{-I_{rs0} z_r}{V_g - v_{out} - v_{Cr0}}\right) + \pi \right]. \tag{7}$$

The following convention for this time interval is established.

$$\beta = t_1 - t_0. \tag{8}$$

ModeII [t_1 t_2]: Once meeting zero, the inductor current flows in the circuit in the reverse direction, making the antiparallel diodes of the switches S1 and S4 forward-biased. The differential equations related to this time interval are given below.

$$V_g = L_r \frac{dI_{rs}(t)}{dt} + v_{Cr}(t) - v_{out}, \tag{9}$$

$$I_{rs}(t) = -C_r \frac{dv_{Cr}(t)}{dt}. \tag{10}$$

By solving (9) and (10), the inductor current I_{rs}, and the capacitor voltage v_{Cr} in this mode of operation is derived.

$$\begin{aligned} I_{rs}(t) =&(2v_{out}+(V_g-v_{Cr0}-v_{out})cos(w_r t_1) \\ &-I_{rs0}z_r sin(w_r t_1))\frac{1}{z_r}sin(w_r t), \end{aligned} \tag{11}$$

$$\begin{aligned} v_{cr}(t) =&V_g+v_{out}+(-2v_{out}-(V_g-v_{out}-v_{Cr0}) \\ &cos(w_r t_1)+I_{rs0}z_r sin(w_r t_1))cos(w_r t). \end{aligned} \tag{12}$$

Since this phase of operation ends when the other pair of switches, S_2 and S_3, are turned on, the duration of this time interval denoted by α is:

$$\alpha = \frac{1}{2f_s}-\beta. \tag{13}$$

In (13), f_s defines the switching frequency of the converter. Demonstrated in 3, the inductor current and capacitor voltage waveforms periodically repeat in each switching cycle. Therefore, these two elements are the potential candidates for being the states of the system. Meanwhile, the extraction of the third equation in terms of the output ($I_{out,rectified}$) and the control input (f_s) is required. For simplicity, the effect of the output filter is ignored as its dynamic behavior is slower than that of the resonant tank. This means that the DC component of the output current is only considered. Concerning the DC component of the output rectified current depicted in Fig. 3, the average output current could be obtained.

$$\begin{aligned} I_{out,rectified} =&\frac{1}{\gamma}(\int_0^{\beta} I_{rs}(t)dt+\int_0^{\alpha} I_{rs}(t)dt) \\ =&\frac{1}{\gamma}\{[\frac{-1}{z_r}(V_g-v_{Cr0}-v_{out})(cos(w_r\beta)-1) \\ &+I_{rs0}sin(w_r\beta)]+\frac{1}{z_r}[2v_{out}+(V_g-v_{Cr0} \\ &-v_{out})cos(w_r\beta)-I_{rs0}z_r sin(w_r\beta)] \\ &(cos(w_r\alpha)-1))\}, \end{aligned} \tag{14}$$

where γ is defined as follows:

$$\gamma = \alpha+\beta. \tag{15}$$

This time period is defined as an event that occurs twice in each switching cycle.

III. Small Signal Analysis

A. Nonlinear Model of the SRC

In this section, the large signal continuous model obtained in the previous section is discretized over the operating point. From Fig. 3, it is apparent that the initial and the final values for the inductor current and the capacitor voltage are the same but mirrored in each event. As an instance, the inductor current in the commencement of the k_{th} meets the same value but with the negative sign in the $(k+1)_{th}$ event. Therefore, the discrete state variables are defined as:

$$\begin{aligned} x_1 &= I_{rs,0(k)} = -I_{rs,0(k+1)} = I_{rs0}, \\ x_2 &= v_{Cr,0(k)} = -v_{C_r,0(k+1)} = v_{Cr0}. \end{aligned} \tag{16}$$

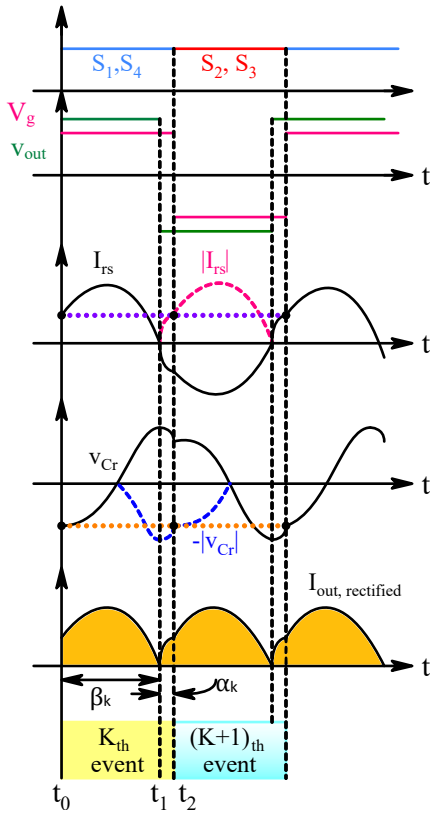

Fig. 3. Key waveforms of the converter.

Given the convention established and used in (16), the discrete values for the inductor current and the capacitor voltage are defined by the means of $I_{rs},j(k)$ and $V_{cr},j(k)$, respectively; where the subscript j represents the time within a certain event and subscript (k) indicates the k_{th} event. By using these discrete start and end point values, the following equations are derived, which end up with the values for inductor current and capacitor voltage at the time t_2.

$$\begin{aligned} I_{rs,2(k)} =&[2v_{out,0(k)}+(V_{g,0(k)}-v_{Cr,0(k)}-v_{out,0(k)}) \\ &cos(w_r\beta)-I_{rs,0(k)}z_r sin(w_r\beta)]\frac{1}{z_r}sin(w_r\alpha), \end{aligned} \tag{17}$$

$$\begin{aligned} v_{cr,2(k)} =&[-2v_{out,0(k)}-(V_{g,0(k)}-v_{out,0(k)} \\ &-v_{Cr,0(k)})cos(w_r\beta)+I_{rs0}z_r sin(w_r\beta)]cos(w_r\alpha) \\ &+V_{g,0(k)}+v_{out,0(k)}, \end{aligned} \tag{18}$$

$$V_{g,0(k)} = V_g, V_{out,0(k)} = V_o. \tag{19}$$

The slopes of the lines connecting the initial values in the $(k+1)_{th}$ event to the same points in the $(k)_{th}$ event could be obtained by the derivative definition as follows:

$$\dot{x} = \frac{x_{i(k+1)}-x_{i(k)}}{t_{i(k+1)}-t_{i(k)}}. \tag{20}$$

TABLE I

PARAMETERS SPECIFICATIONS

Nominal power	10 MW
Nominal input Voltage (V_g)	2 kV
Nominal output Voltage (V_o)	50 kV
Resonant inductor (L_r)	78 mH
Resonant capacitor (C_r)	0.25 μF
Magnetizing inductance (L_m)	10 mH
Nominal switching frequency (f_s)	1000 Hz
Range of switching frequency deviation	$\pm$100 Hz
n	25

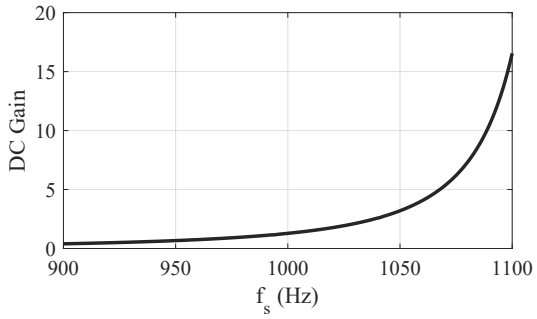

Fig. 4. DC gain of the transfer function $G_{f_s \to I_{out}}$ for different switching frequencies.

Using (16), (17) and (18) and substituting in (20) results in nonlinear state equations.

$$\begin{aligned}\dot{x_1} =& 2f_s\{[sin(w_r\beta)sin(w_r\alpha)-1]x_1 \\ &+[sin(w_r\alpha)cos(w_r\beta)]\frac{x_2}{z_r} \\ &+[-2sin(w_r\alpha)+cos(w_r\beta)sin(w_r\alpha)]\frac{v_{out,0(k)}}{z_r} \\ &+[-cos(w_r\beta)sin(w_r\alpha)]\frac{V_{in,0(k)}}{z_r} \\ =& f_1(x_1,x_2,f_s,V_{g,0(k)},v_{out,0(k)}) = f_1(x_1,x_2,V_g,v_{out}),\end{aligned} \tag{21}$$

$$\begin{aligned}\dot{x_2} =& 2f_s\{[z_r sin(w_r\beta)cos(w_r\alpha)]x_1 \\ &+[cos(w_r\beta)cos(w_r\alpha)+1]x_2 \\ &+[-2cos(w_r\alpha)+cos(w_r\alpha)cos(w_r\beta)+1]v_{out,0(k)} \\ &+[-cos(w_r\alpha)cos(w_r\beta)+1]V_{g,0(k)} \\ =& f_2(x_1,x_2,f_s,V_{g,0(k)},v_{out,0(k)}) = f_2(x_1,x_2,V_g,v_{out}).\end{aligned} \tag{22}$$

Applying the notations defined in (16) to the (14), similarly, generates the function relating the state vectors and inputs to the output rectified current.

$$\begin{aligned}I_{out,rectified} =& \frac{1}{\gamma}\{[\frac{-1}{z_r}(V_{in,0(k)}-x_2-v_{out,0(k)}) \\ &(cos(w_r\beta)-1))+x_1 sin(w_r\beta)] \\ &+\frac{1}{z_r}[2v_{out,0(k)}+(V_{in,0(k)}-x_2-v_{out,0(k)}) \\ &cos(w_r\beta)-x_1 z_r sin(w_r\beta)](cos(w_r\alpha)-1))\} \\ =& f_3(x_1,x_2,V_{in,0(k)},v_{out,0(k)}) = f_3(x_1,x_2,V_{in},v_{out}).\end{aligned} \tag{23}$$

The parameters specifications for a layer of MVDC converter used for offshore wind farm applications are presented in table I [2].

B. Linearized model of the SRC

In this section, the plant dynamic is analytically approximated through the differential equation in the vicinity of the equilibrium point where (24) is satisfied.

$$\dot{X} = f_1(x_1,x_2,V_g,V_{out}) = f_2(x_1,x_2,V_g,V_{out}) = 0. \tag{24}$$

Then, the linearized state equation of the plant around the trim point could be generated.

$$\begin{aligned}\frac{d}{dt}\Delta X(t) &= A\Delta X + B\Delta u, \\ \Delta y(t) &= \Delta I_{out,rectified} = C\Delta X + D\Delta u,\end{aligned} \tag{25}$$

where ΔX, Δu, and Δy, respectively, represent the small deviations of the state vector, input vector, and rectified output current. Moreover, A, B, C, and D are the matrices with the corresponding dimensions. These matrices are computed through the Jacobian matrix at the trim values. These values are not unique in the case of the MVDC converter, but only one of the equilibrium points is acceptable from the experimental point of view. Concerning the dimension of the linearized matrix, the multiple-input single-output (MISO) system forms three transfer functions, namely, $G_{V_{in}\to I_{out}}(s)$, $G_{v_{out}\to I_{out}}(s)$ and $G_{f_s\to I_{out}}(s)$ given in (26); where the first two transfer functions describe the system's response to the input and output voltage disturbances that might happen, whereas the last transfer function demonstrates how the output current changes if the control input is changed. It should be mentioned that these equations are the descriptions of the system's behavior when operating at the nominal switching frequency.

$$\begin{aligned}G_{V_{in}\to I_{out}}(s) &= \frac{0.0009s^2+5.6s+7164}{s^2+1300s+5.6e05}, \\ G_{v_{out}\to I_{out}}(s) &= \frac{-0.0008s^2-6.8s-5560}{s^2+1300s+5.6e05}, \\ G_{f_s\to I_{out}}(s) &= \frac{0.09s^2+181.9s+7.2e05}{s^2+1300s+5.6e05},\end{aligned} \tag{26}$$

The poles of the plant, which are $-648.84 \pm j380.94$, indicate that the plant exhibits an underdamped response to a step input. This means that the output of the systems oscillates before settling to its final value. Moreover, Fig. 4 illustrates the changes in the gain values as the frequency changes. This observation suggests the possibility of a bifurcation phenomenon. The presence of this phenomenon in the behavior of the system implies that even small variations in the systems's behavior can lead to qualitative changes in its response. Therefore, to ensure stability and consistent performance of the system under these changing conditions, a gain scheduling controller is justified. This type of controller can adapt the system's gain based on the current operating conditions, compensating for the variations in the plant parameters and maintaining stability and desired performance.

TABLE II

PARAMETERS SPECIFICATIONS OF THE SCALED CONVERTER

Inverter Bridge	2×imperix PEB 4046-A
Bridge rectifier	KMB245S
Nominal input Voltage (V_g)	2 V
Nominal output Voltage (V_o)	1 V
Resonant inductor (L_r)	50 mH
Resonant capacitor (C_r)	0.27 μF
Nominal switching frequency (f_s)	1200 Hz
Range of switching frequency deviation	±1100 Hz-1500 Hz
n	1

IV. MODEL VERIFICATION

A. Simulation Results

In this section, the Bode diagram of the linearized model alongside a circuit diagram is presented. For this purpose, a sinusoidal waveform with a constant bias is applied to the inverter as the switching frequency. The switching frequency is therefore represented by a sine wave with a specific range of frequencies, which forms the frequency axis of the bode diagram. Fig.5 compares the Bode diagram of the mathematical model and the circuit. This shows that the magnitudes and phase diagrams of the linearized model and circuit are in agreement. An important factor to consider is that the sinusoidal waveform's frequency should not exceed %10 of the switching frequency. Exceeding this limit would introduce harmonics in the output current, rendering the derivation of the phase difference between the switching frequency and the output waveforms meaningless. Additionally, it becomes complicated to determine system gain in the presence of such harmonics. Hence, it is necessary for the bandwidth of the controller designed for this converter to be narrower than the aforementioned frequency range. As a result of restricting the controller's bandwidth, the control system exhibits a lower gain at frequencies that correspond to the harmonics introduced by the sinusoidal waveform. This, therefore, helps in surpassing the effects of the harmonics and maintaining system stability.

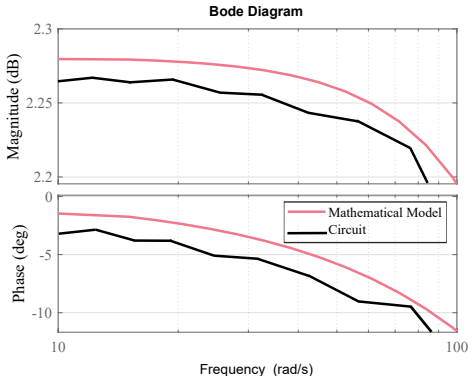

Fig. 5. Comparison between the bode diagrams derived from the mathematical model and the circuit.

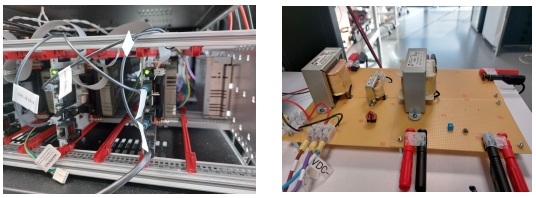

(a) (b)

Fig. 6. Scaled prototype of the converter (a) Full-bridge inverter (c) The rest of the converter connected to the inverter.

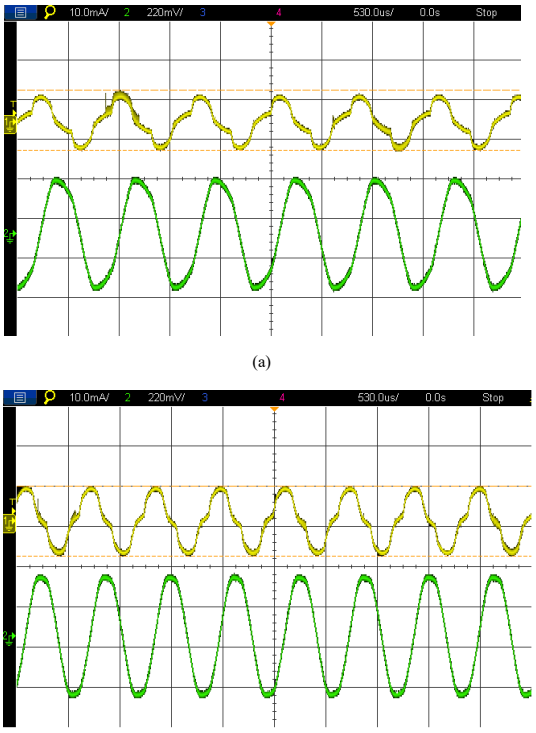

(a)

(b)

Fig. 7. Inductor current and the capacitor voltage measured by scope; (a) f_s=1.2KHz and (b) f_s=1.5KHz.

B. Experimental Verification

Provided in Fig. 6 is a scaled prototype with the specifications given in table II. In this section, the experimentally obtained results are compared with the theoretically calculated values to confirm the validity of the nonlinear model. Regarding the experimental analysis, it should be noted that the differential probe used to measure the capacitor voltage has a turn ratio of 10:1, which makes the voltage ten times smaller. As expected and shown in Fig.7, the inductor current and capacitor voltage individually experience a curvature in each half of the switching cycle and it occurs periodically. These two points where the curvatures appear are the key points based on which the model is linearized. It is of importance to mention that the values for the curvatures depend on the switching frequency; that is, the equilibrium point changes with the switching frequency deviations. This, in turn, verifies what was expressed pertaining to the bifurcation phenomena. Moreover, it is apparent that as the switching

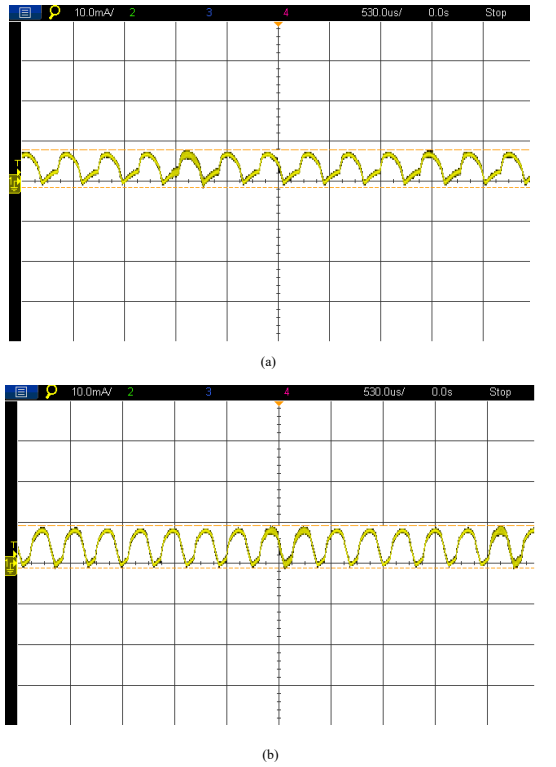

Fig. 8. Rectified current pulses injected in the grid measured by scope; (a) f_s=1.2KHz and (b) f_s=1.5KHz.

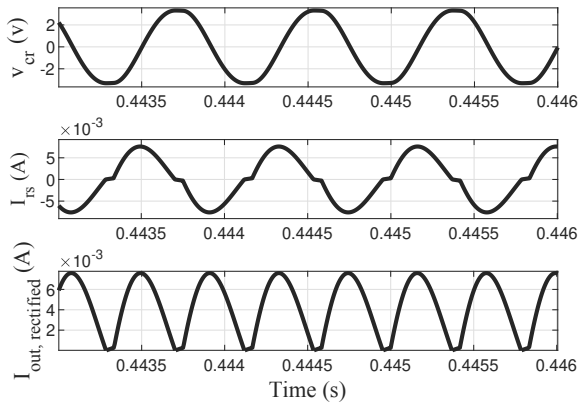

Fig. 9. Theoretically obtained waveforms of the scaled model of the SRC operating at 1.2KHz.

frequency increases by up to the resonant frequency, more current pulses are transmitted to the load. Consequently, the output power is a function of switching frequency, shown in Fig. 8.

To verify the experimental results and show that they are consistent with the theoretically calculated values, the capacitor voltage, and the inductor current waveforms for the scaled model are shown in Fig. 9. As can be seen, the capacitor voltage and the inductor current witness nearly the same waveforms as the ones shown in Fig. 7 and Fig. 8. However, it should be borne in mind that the duration of the first operating mode (α) in the mathematical analysis is negligibly less than what it practically is and the main reason behind this is the inductance of the transformer. As assumed in advance, the transformer is ideal, but it, practically, has a leakage inductance that affects the resonant frequency.

V. CONCLUSIONS

In this paper, an SRC suitable for high-power medium-voltage applications is modeled through the discrete-time-domain modeling approach. The nonlinear alongside the linearized models of the converter are obtained and the accuracy is verified via the comparison of the simulated converter and mathematical model. Furthermore, a scaled prototype is implemented and the experimentally obtained waveforms are compared with the theoretically calculated waveforms to confirm the validity of the analysis.

REFERENCES

[1] C. Dincan, P. Kjaer, Y.-h. Chen, S. Munk-Nielsen, and C. L. Bak, "A high-power, medium-voltage, series-resonant converter for dc wind turbines," *IEEE Transactions on Power Electronics*, vol. 33, no. 9, pp. 7455–7465, 2017.

[2] C. G. Dincan, P. Kjaer, Y.-H. Chen, E. Sarrá-Macia, S. Munk-Nielsen, C. L. Bak, and S. Vaisambhayana, "Design of a high-power resonant converter for dc wind turbines," *IEEE Transactions on Power Electronics*, vol. 34, no. 7, pp. 6136–6154, 2019.

[3] L. A. D. Ta, N. D. Dao, and D.-C. Lee, "High-efficiency hybrid llc resonant converter for on-board chargers of plug-in electric vehicles," *IEEE Transactions on Power Electronics*, vol. 35, no. 8, pp. 8324–8334, 2020.

[4] F. Degioanni, I. G. Zurbriggen, and M. Ordonez, "Dual-loop controller for llc resonant converters using an average equivalent circuit," in *2017 IEEE Energy Conversion Congress and Exposition (ECCE)*, 2017, pp. 230–236.

[5] M. Mohammadi, F. Degioanni, M. Mahdavi, and M. Ordonez, "Small-signal modeling of llc converters using homopolarity cycle," *IEEE Transactions on Power Electronics*, vol. 35, no. 4, pp. 4076–4093, 2020.

[6] B. Cheng, F. Musavi, and W. G. Dunford, "Novel small signal modeling and control of an llc resonant converter," in *2014 IEEE Applied Power Electronics Conference and Exposition-APEC 2014*. IEEE, 2014, pp. 2828–2834.

[7] J. Stahl, T. Hieke, C. Oeder, and T. Duerbaum, "Small signal analysis of the resonant llc converter," in *2013 IEEE ECCE Asia Downunder*. IEEE, 2013, pp. 25–30.

[8] T. Duerbaum, "First harmonic approximation including design constraints," in *INTELEC - Twentieth International Telecommunications Energy Conference (Cat. No.98CH36263)*, 1998, pp. 321–328.

[9] C.-H. Chang, E.-C. Chang, C.-A. Cheng, H.-L. Cheng, and S.-C. Lin, "Small signal modeling of llc resonant converters based on extended describing function," in *2012 International Symposium on Computer, Consumer and Control*. IEEE, 2012, pp. 365–368.

[10] S. Tian, F. C. Lee, and Q. Li, "Equivalent circuit modeling of llc resonant converter," *IEEE Transactions on Power Electronics*, vol. 35, no. 8, pp. 8833–8845, 2020.

[11] R. King and T. Stuart, "Small-signal model for the series resonant converter," *IEEE transactions on aerospace and electronic systems*, no. 3, pp. 301–319, 1985.

[12] Y.-H. Chen, C. G. Dincan, P. Kjær, C. L. Bak, X. Wang, C. E. Imbaquingo, E. Sarrà, N. Isernia, and A. Tonellotto, "Model-based control design of series resonant converter based on the discrete time domain modelling approach for dc wind turbine," *Journal of Renewable Energy*, vol. 2018, 2018.